GEOPHYSICS, VOL. 71, NO. 5 (SEPTEMBER-OCTOBER 2006); P. G225–G233, 12 FIGS.
10.1190/1.2245467

Finite-difference simulation of borehole EM measurements in 3D anisotropic media using coupled scalar-vector potentials

Junsheng Hou[1], Robert K. Mallan[1], and Carlos Torres-Verdín[1]

ABSTRACT

This paper describes the implementation and successful validation of a new staggered-grid, finite-difference algorithm for the numerical simulation of frequency-domain electromagnetic borehole measurements. The algorithm is based on a coupled scalar-vector potential formulation for arbitrary 3D inhomogeneous electrically anisotropic media. We approximate the second-order partial differential equations for the coupled scalar-vector potentials with central finite differences on both Yee's staggered and standard grids. The discretization of the partial differential equations and the enforcement of the appropriate boundary conditions yields a complex linear system of equations that we solve iteratively using the biconjugate gradient method with preconditioning. The accuracy and efficiency of the algorithm is assessed with examples of multicomponent-borehole electromagnetic-induction measurements acquired in homogeneous, 1D anisotropic, 2D isotropic, and 3D anisotropic rock formations. The simulation examples consider vertical and deviated wells with and without borehole and mud-filtrate invasion regions. Simulation results obtained with the scalar-vector coupled potential formulation favorably compare in accuracy with results obtained with 1D, 2D, and 3D benchmarking codes in the dc to megahertz frequency range for large contrasts of electrical conductivity. Our numerical exercises indicate that the coupled scalar-vector potential equations provide a general and consistent algorithmic formulation to simulate borehole electromagnetic measurements from dc to megahertz in the presence of large conductivity contrasts, dipping wells, electrically anisotropic media, and geometrically complex models of electrical conductivity.

INTRODUCTION

Several electromagnetic (EM) finite-difference (FD) algorithms have been developed to simulate subsurface geophysical measurements acquired in 3D environments (see, for example, Smith, 1996; LaBrecque, 1999; Haber and Ascher, 2001; Wang and Fang, 2001; Newman and Alumbaugh, 2002; Davydycheva et al., 2003; Hou and Torres-Verdín, 2003; and Weiss and Newman, 2003). There are two main alternatives for solving the boundary-value problem of Maxwell's equations using finite differences: (1) to discretize the second-order partial differential equations (PDEs) governing electric or magnetic fields (referred to as direct EM field formulations or EM field formulations) and (2) to discretize the second-order PDEs governing the vector and scalar potentials (referred to as EM potential formulation or potential formulation).

It is common practice to solve EM boundary-value problems using auxiliary scalar-vector potentials. In the past, EM potential formulations have been used for FD modeling in the low-frequency regime. LaBrecque (1999) derived a coupled scalar-vector potential formulation using the central FD standard grid for the case of isotropic media; he discussed the nature of spurious modes arising with the use of naive EM field formulations. Haber and Ascher (2001) and Haber et al. (2000, 2002) used coupled potentials for computing frequency- and time-domain EM responses in isotropic media; they showed that the coupled potential method entailed shorter computation times than the electric field method.

Direct EM-field formulations indirectly make use of scalar potentials to stabilize low frequency calculations. For instance, Smith (1996) developed a static divergence correction for the direct electric-field formulation using a single dc scalar potential function. Numerical tests showed that Smith's (1996) correction method drastically improved the rate of convergence of the simulation algorithm at low frequencies. Druskin et al. (1999) used the decoupled vector and dc scalar potential functions for the computation of an inverse Maxwell operator in conjunction with their spectral Lanczos decomposition method (SLDM) of the electric field formulation in isotropic media. Newman and Alumbaugh (2002) developed an FD algo-

Manuscript received by the Editor June 30, 2004; revised manuscript received March 11, 2006; published online August 28, 2006.
[1]The University of Texas at Austin, Department of Petroleum and Geosystems Engineering, Austin, Texas. Presently Halliburton Energy Services. E-mail: junsheng63@yahoo.com; cverdin@mail.utexas.edu; rkmallan@mail.utexas.edu.

rithm using the decoupled vector potential and dc scalar potential functions similar to that used by Druskin et al. (1999) for the case of anisotropic media. Finally, Weiss and Newman (2003) improved the direct field corrected algorithm of Newman and Alumbaugh (2002) for the case of a generalized anisotropic medium.

Scalar-vector potential formulations exhibit some obvious advantages compared to direct EM-field modeling. For example, they explicitly overcome the problem of spurious modes resulting from the use of the "curl-curl" operator of direct fields at low frequencies. Because of this, scalar-vector potential formulations provide stable results over a broad frequency range.

In this paper, we adopt a coupled scalar-vector potential formulation similar to that of LaBrecque (1999) and develop an algorithm for FD simulation of EM fields on both Yee's staggered and standard grids using the second-order coupled scalar-vector potential PDEs in 3D inhomogeneous, electrically anisotropic media. We apply this algorithm to the simulation of borehole EM logging measurements with multicomponent magnetic transmitters and receivers.

In the following sections, starting from the frequency-domain Maxwell's equations, we first derive the PDEs for coupled scalar-vector potentials in arbitrary 3D electrically anisotropic inhomogeneous media. Next, we introduce the FD method on the staggered standard grid to discretize the continuous governing equations and use a preconditioned complex biconjugate gradient method (CBCG) to solve the ensuing complex linear system of equations. Finally, we benchmark the validity and accuracy of the new algorithm against 1D anisotropic, 2D isotropic, and 3D anisotropic solutions.

METHODOLOGY

The EM forward model considered in this paper consists of solving Maxwell's equations in the frequency domain and assumes a time-harmonic variation of the form $e^{i\omega t}$, where t is time, $i = \sqrt{-1}$, $\omega = 2\pi f$ is angular frequency, and f is linear frequency (Hz). For arbitrary 3D, inhomogeneous, electrically anisotropic media and assuming SI units, Maxwell's equations in the presence of impressed electric current sources are given by

$$\nabla \times \mathbf{E} = -i\omega\mu_0\mathbf{H}, \tag{1}$$

$$\nabla \times \mathbf{H} = \bar{\bar{\sigma}}'\mathbf{E} + \mathbf{J}_p, \tag{2}$$

and

$$\nabla \cdot \mathbf{B} = 0, \tag{3}$$

where $\mathbf{E}$ and $\mathbf{H}$ are the electric- and magnetic-field vectors, respectively, and $\mathbf{B}$ is the magnetic flux density vector. We assume that the medium under consideration does not exhibit spatial variations of magnetic permeability, whereupon the magnetic field and flux density are related by $\mathbf{B} = \mu_0\mathbf{H}$, where $\mu_0 = 4\pi \times 10^{-7}$(H/m) is the magnetic permeability of free space. In equation 2, $\mathbf{J_p}$ is the impressed electrical-source-current density vector, $\bar{\bar{\sigma}}' = \bar{\bar{\sigma}} + i\omega\bar{\bar{\varepsilon}}$ is the complex conductivity tensor, $\bar{\bar{\sigma}}$ is the ohmic conductivity tensor, ε is dielectric permittivity, and $\bar{\bar{\mathbf{I}}}$ is the unity dyad.

From equation 3, we can express the magnetic flux density in the form

$$\mathbf{B} = \nabla \times \mathbf{A},$$

where $\mathbf{A}$ is a vector potential that satisfies the Coulomb gauge, i.e.,

$$\nabla \cdot \mathbf{A} = 0.$$

The vector function $\mathbf{A}$ above is referred to as the magnetic vector potential (van Bladel, 1985; King and Prasad, 1986). Substitution of the above identities into Maxwell's equations 1 and 2 gives rise to the expressions

$$\mathbf{H} = (1/\mu_0)\nabla \times \mathbf{A}, \tag{4}$$

$$\mathbf{E} = -i\omega\mathbf{A} - \nabla V, \tag{5}$$

$$\nabla^2\mathbf{A} - i\omega\mu_0\bar{\bar{\sigma}}'\mathbf{A} - \mu_0\bar{\bar{\sigma}}' \cdot \nabla V = -\mu_0\mathbf{J}_p, \tag{6}$$

and

$$i\omega\nabla \cdot (\bar{\bar{\sigma}}'\mathbf{A}) + \nabla \cdot (\bar{\bar{\sigma}}' \cdot \nabla V) = \nabla \cdot \mathbf{J}_p, \tag{7}$$

where V is the (total) electric scalar potential. The above expressions are the PDEs governing the coupled scalar-vector potentials. For the case of isotropic electrical conductivity, equations 6 and 7 are equivalent to those used by LaBrecque (1999).

Equations 6 and 7 are defined over an unbounded spatial domain $\Omega = R^3$. In practice, however, a bounded subdomain of Ω is used to perform the numerical simulation. In our formulation, we enforce homogeneous Dirichlet boundary conditions (for example, $\mathbf{n} \times \mathbf{A}|_{\partial\Omega} = 0$ and $V|_{\partial\Omega} = 0$, where $\partial\Omega$ is the outer boundary of the domain, and $\mathbf{n}$ is the outer normal unit vector of the boundary $\partial\Omega$) and mixed-boundary conditions for coupled potentials.

Next, let us assume that the complex conductivity $\bar{\bar{\sigma}}'$ is a symmetric and nonnegative 3×3 tensor given by

$$\bar{\bar{\sigma}}' = \bar{\bar{\sigma}}'(x,y,z) = \begin{pmatrix} \sigma'_{xx} & \sigma'_{xy} & \sigma'_{xz} \\ \sigma'_{yx} & \sigma'_{yy} & \sigma'_{yz} \\ \sigma'_{zx} & \sigma'_{zy} & \sigma'_{zz} \end{pmatrix},$$

which exhibits only six independent entries. We express the coupled PDEs 6 and 7 in terms of individual Cartesian components as follows:

$$\nabla^2 A_x - i\omega\mu_0(\sigma'_{xx}A_x + \sigma'_{xy}A_y + \sigma'_{xz}A_z) - \left(\sigma'_{xx}\frac{\partial V}{\partial x} + \sigma'_{xy}\frac{\partial V}{\partial y} + \sigma'_{xz}\frac{\partial V}{\partial z}\right) = -\mu_0 J_{px}, \tag{8}$$

$$\nabla^2 A_y - i\omega\mu_0(\sigma'_{yx}A_x + \sigma'_{yy}A_y + \sigma'_{yz}A_z) - \left(\sigma'_{yx}\frac{\partial V}{\partial x} + \sigma'_{yy}\frac{\partial V}{\partial y} + \sigma'_{yz}\frac{\partial V}{\partial z}\right) = -\mu_0 J_{py}, \tag{9}$$

$$\nabla^2 A_z - i\omega\mu_0(\sigma'_{zx}A_x + \sigma'_{zy}A_y + \sigma'_{zz}A_z) - \left(\sigma'_{zx}\frac{\partial V}{\partial x} + \sigma'_{zy}\frac{\partial V}{\partial y} + \sigma'_{zz}\frac{\partial V}{\partial z}\right) = -\mu_0 J_{pz}, \tag{10}$$

and

$$i\omega\left\{\frac{\partial}{\partial x}[\sigma'_{xx}A_x+\sigma'_{xy}A_y+\sigma'_{xz}A_z]+\frac{\partial}{\partial y}[\sigma'_{yx}A_x+\sigma'_{yy}A_y+\sigma'_{yz}A_z]+\frac{\partial}{\partial z}[\sigma'_{zx}A_x+\sigma'_{zy}A_y+\sigma'_{zz}A_z]\right\}+\frac{\partial}{\partial x}\left[\sigma'_{xx}\frac{\partial V}{\partial x}+\sigma'_{xy}\frac{\partial V}{\partial y}+\sigma'_{xz}\frac{\partial V}{\partial z}\right]+\frac{\partial}{\partial y}\left[\sigma'_{yx}\frac{\partial V}{\partial x}+\sigma'_{yy}\frac{\partial V}{\partial y}+\sigma'_{yz}\frac{\partial V}{\partial z}\right]+\frac{\partial}{\partial z}\left[\sigma'_{zx}\frac{\partial V}{\partial x}+\sigma'_{zy}\frac{\partial V}{\partial y}+\sigma'_{zz}\frac{\partial V}{\partial z}\right]=\nabla\cdot\mathbf{J}_p,\frac{\partial\mathbf{J}_{px}}{\partial_x}+\frac{\partial\mathbf{J}_{py}}{\partial_y}+\frac{\partial\mathbf{J}_{pz}}{\partial_z} \tag{11}$$

where J_{px}, J_{py}, and J_{pz} are the Cartesian components of the impressed source current in the x-, y-, and z-directions, respectively, and A_x, A_y, and A_z are the Cartesian components of the vector potential in the x-, y-, and z-directions, respectively.

To solve the 3D boundary-value problem of coupled scalar-vector potentials with the FD method, the solution domain is divided into $\mathbf{N}_x \times \mathbf{N}_y \times \mathbf{N}_z$ rectangular cells in the Cartesian coordinate system. We employ a central FD approximation on both a Yee staggered grid (Yee, 1966) and a standard grid. As Figure 1 illustrates, the three components of the vector potential **A** sampled on Yee's staggered grid are located at the center of the edges of the cell, whereas the scalar potential V is sampled on a standard grid at the corner of the cell. Finite-difference forms of equations 8–10 are obtained by performing the volume integral over the region surrounding each node; using the divergence theorem, the finite-difference form of equation 11 is obtained by performing the surface integral over the volume region encompassing each node. Averaged conductivities and potential components, which are not defined on the same grid points in the FD equations, are calculated using methods similar to the ones described by Wang and Fang (2001) and Weiss and Newman (2002, 2003). Discretization of the coupled scalar-vector potential equations yields four coupled linear systems of equations. We write the fully discretized boundary-value problem with the matrix notation

$$\mathbf{FX}=\mathbf{D}, \tag{12}$$

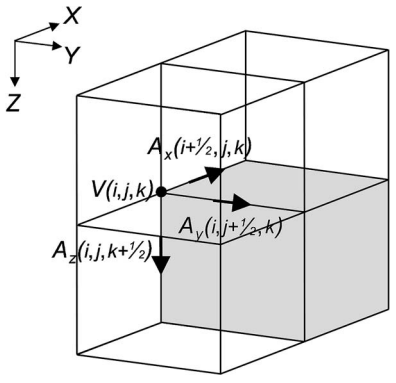

Figure 1. Three-dimensional Cartesian FD stencil showing sampling locations for the vector and scalar potentials on Yee's staggered and standard grids. The three components of the vector potential **A** are located at the center of the cell edges, whereas the scalar potential V is located at the cell corner.

or, equivalently,

$$\begin{pmatrix}\mathbf{S}^1 & \mathbf{S}^2 & \mathbf{S}^3 & \mathbf{S}^4\\ \mathbf{T}^1 & \mathbf{T}^2 & \mathbf{T}^3 & \mathbf{T}^4\\ \mathbf{U}^1 & \mathbf{U}^2 & \mathbf{U}^3 & \mathbf{U}^4\\ \mathbf{W}^1 & \mathbf{W}^2 & \mathbf{W}^3 & \mathbf{W}^4\end{pmatrix}\cdot\begin{pmatrix}\mathbf{A}_x\\ \mathbf{A}_y\\ \mathbf{A}_z\\ \mathbf{V}\end{pmatrix}=\begin{pmatrix}\mathbf{b}_x\\ \mathbf{b}_y\\ \mathbf{b}_z\\ \mathbf{b}_v\end{pmatrix}, \tag{13}$$

where $\mathbf{F}=(a_{ij})_{N\times N}$ is a nonsymmetric four-by-four-block complex matrix. The rows of this matrix contain only a limited number of nonzero entries. Therefore, **F** is a large, sparse, and banded matrix; its entries mainly depend on grid spacing and medium averaged conductivity; N is the total number of the unknowns, with $N = m_1 + m_2 + m_3 + m_4$, $m_1 = N_x \cdot (N_y - 1) \cdot (N_z - 1)$, $m_2 = (N_x - 1) \cdot N_y \cdot (N_z - 1)$, $m_3 = (N_x - 1) \cdot (N_y - 1) \cdot N_z$, and $m_4 = (N_x - 1) \cdot (N_y - 1) \cdot (N_z - 1)$. In equation 12, the vector $\mathbf{X} = (\mathbf{A_x}, \mathbf{A_y}, \mathbf{A_z}, \mathbf{V})^{\mathbf{T}}$ is the unknown vector of complex potential values throughout the discretized model, $\mathbf{D} = (\mathbf{d_x}, \mathbf{d_y}, \mathbf{d_z}, \mathbf{d_v})^{\mathbf{T}}$ is the right-hand vector containing source terms associated with the boundary conditions, the superscript T indicates transpose, and $\mathbf{S}^1$, $\mathbf{S}^2$ $\mathbf{S}^3$, $\mathbf{S}^4$, $\mathbf{T}^1$, $\mathbf{T}^2$, $\mathbf{T}^3$, $\mathbf{T}^4$, $\mathbf{U}^1$, $\mathbf{U}^2$, $\mathbf{U}^3$, $\mathbf{U}^4$, $\mathbf{W}^1$, $\mathbf{W}^2$, $\mathbf{W}^3$, and $\mathbf{W}^4$ are 16 block matrices included in matrix **F** and given by

$\mathbf{S}^1 = (\mathbf{S}^1_{\mathbf{i_1 j_1}})_{\mathbf{m_1}\times\mathbf{m_1}}$, $\mathbf{S}^2 = (\mathbf{S}^2_{\mathbf{i_1 j_2}})_{\mathbf{m_1}\times\mathbf{m_2}}$, $\mathbf{S}^3 = (\mathbf{S}^3_{\mathbf{i_1 j_3}})_{\mathbf{m_1}\times\mathbf{m_3}}$,
$\boldsymbol{S}^4 = (\mathbf{S}^4_{\mathbf{i_1 j_4}})_{\mathbf{m_1}\times\mathbf{m_4}}$,

$$\mathbf{T}^1=(\mathbf{T}^1_{i_2 j_1})_{m_2\times m_1},\quad \mathbf{T}^2=(\mathbf{T}^2_{i_2 j_2})_{m_2\times m_2},$$

$$\mathbf{T}^3=(\mathbf{T}^3_{i_2 j_3})_{m_2\times m_3},\quad \mathbf{T}^4=(\boldsymbol{T}^4_{i_2 j_4})_{m_2\times m_4},$$

$$\mathbf{U}^1=(\mathbf{U}^1_{i_3 j_1})_{m_3\times m_1},\quad \mathbf{U}^2=(\mathbf{U}^2_{i_3 j_2})_{m_3\times m_2},$$

$$\mathbf{U}^3=(\mathbf{U}^3_{i_3 j_3})_{m_3\times m_3},\quad \mathbf{U}^4=(\mathbf{U}^4_{i_3 j_4})_{m_3\times m_4},$$

$$\mathbf{W}^1=(\mathbf{W}^1_{i_4 j_1})_{m_4\times m_1},\quad \mathbf{W}^2=(\mathbf{W}^2_{i_4 j_2})_{m_4\times m_2},$$

$$\mathbf{W}^3=(\mathbf{W}^3_{i_4 j_3})_{m_4\times m_3},\quad \text{and } \mathbf{W}^4=(\mathbf{W}^4_{i_4 j_4})_{m_4\times m_4}.$$

Moreover, $\mathbf{S}^1$, $\mathbf{T}^2$, $\mathbf{U}^3$, and $\mathbf{W}^4$ are block-symmetric matrices with $\mathbf{S}^2 = (\mathbf{T}^1)^{\mathbf{T}}$, $\mathbf{S}^3 = (\mathbf{U}^1)^{\mathbf{T}}$, and $\mathbf{T}^3 = (\mathbf{U}^2)^{\mathbf{T}}$. When the conductivity tensor is diagonal, matrix **F** becomes sparse and doubly bordered block diagonal.

From the derivation above, it follows that the EM forward-modeling problem with coupled scalar-vector potentials reduces to solving the discretized linear system 13. Because this linear system is nonsymmetric and complex valued, we iteratively solve it using the complex biconjugate gradient algorithm (CBCG). To accelerate its iterative rate of convergence, we precondition the linear system before attempting its solution. Therefore, we refer to the overall solution scheme as the preconditioned complex biconjugate gradient algorithm, or PBCG. We have used different preconditioning methods, including Jacobi, symmetric successive overrelaxation (SSOR), and incomplete LU decomposition (ILU) (Axelsson, 1994). Appendix A graphically describes the convergence properties of these preconditioning methods for one of the example prob-

lems subsequently considered in this paper. We enforce a convergence criterion with the l_p-norm formula

$$\frac{\|\mathbf{FX} - \mathbf{D}\|_p}{\|\mathbf{D}\|_p} < \varepsilon, \tag{14}$$

where ε is the threshold value for the iterative error and p is a positive integer. The iterations are continued until the termination condition (equation 14) is satisfied. Values of ε used in the literature usually range from 10^{-4} to 10^{-7}. Our numerical experiments indicate that $\varepsilon = 10^{-6} - 10^{-7}$ and $p = 2$ are satisfactory choices.

NUMERICAL RESULTS

We now apply the 3D FD coupled scalar-vector potential algorithm described above to simulate multicomponent-borehole EM induction-logging measurements acquired across a complex-reservoir model with permeable and impermeable layers. First, we perform an evaluation of the algorithm by comparing results against independent 1D, 2D, and 3D solutions over a suite of variations of the main model.

Figure 2 shows the resistivity model considered for the numerical comparison; it consists of a sequence of reservoir layers — ranging from conductive brine bearing to resistive hydrocarbon bearing — shouldered by conductive shale layers. This model was adapted from an actual borehole-logging situation, a dipping well located in Gulf of Mexico deep water and penetrating Tertiary unconsolidated turbidite sediments. It includes a wide range of variations of conductivity/resistivity contrasts. Particular emphasis is given to the presence of electrical anisotropy in shales shouldering porous and permeable sands, and to its influence on measurements across the reservoir layers under variations of dip angle, layer thickness, and radial length of invasion. We simulate the measurements assuming a tool that consists of a multicomponent magnetic receiver collocated with and 1.8 m below a single multicomponent magnetic transmitter operating at 25, 50, and 100 kHz (Figure 3). Simulated magnetic fields are denoted as $H_{pq} = \mathrm{Re}(H_{pq}) + i\,\mathrm{Im}(H_{pq})$, where $\mathrm{Re}(H_{pq})$ and $\mathrm{Im}(H_{pq})$ are the real (in-phase) and imaginary (quadrature) parts of the magnetic field, respectively, the subscript p indicates the moment orientation of the magnetic transmitter, and the subscript q indicates the orientation of the magnetic receiver. In this paper we only consider magnetic field components of the type $H_{pp} = \mathrm{Re}(H_{pp}) + i\,\mathrm{Im}(H_{pp})$ for the simulation examples. For instance, $\mathrm{Im}(H_{zz})$ and $\mathrm{Re}(H_{zz})$ are the quadrature and in-phase components of the vertical magnetic field H_{zz}, respectively, excited by a z-directed magnetic dipole transmitter. Moreover, for the sake of brevity, in the majority of the simulations presented here we show only results for the quadrature component.

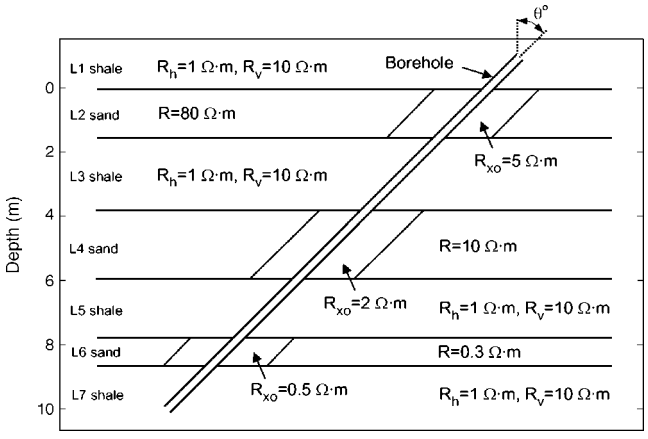

Figure 2. Layered resistivity model with borehole and invasion. Diameters of the borehole and invasion are 21.59 cm and 30.48 cm, respectively. The borehole resistivity is 0.4 ohm-m, with the borehole dip angle located in the x-z Cartesian plane. Length (and dimensions) along the horizontal axis correspond to projected distances that depend on specific values of dip angle.

We make use of a nonuniform Cartesian grid around the transmitter and receiver, with a minimum grid size of 0.05 m near the transmitter and the receiver. Grid steps progressively increase outward from transmitter/receiver locations with incremental steps, as described by Davydycheva et al. (2003), to the outer boundary located one to two skin depths away for the lowest frequency of interest. A homogeneous zero Dirichlet boundary condition is enforced at the outer grid nodes. The layered formation model shown in Figure 2, with borehole and invasion, is superimposed onto the grid using the standard homogenization, conductivity-averaging approach described by Moskow et al. (1999). In the simulation examples, the grid size consists of $28 \times 28 \times 92$ cells in the x-, y-, and z-directions, respectively. Figure 3 shows the distribution of grid nodes in the x-z Cartesian plane superimposed to one of the layers included in Figure 2, dipping at an angle of 60°. The same figure shows the relative location of the transmitter and receiver. We "transport" this Cartesian grid from one measurement point to another as the location of the tool is progressively moved along the borehole axis to reproduce a standard logging operation.

The first benchmark exercise is a 1D simulation of the layered structure shown in Figure 2, without borehole and invasion, for a measurement profile at 60° from the direction normal to the layers. Figures 4 and 5 compare the Hzz, Hxx, and Hyy in-phase and quadrature field responses, respectively, simulated with 3D coupled scalar-vector algorithm and a 1D analytical solution (Lu and Alum-

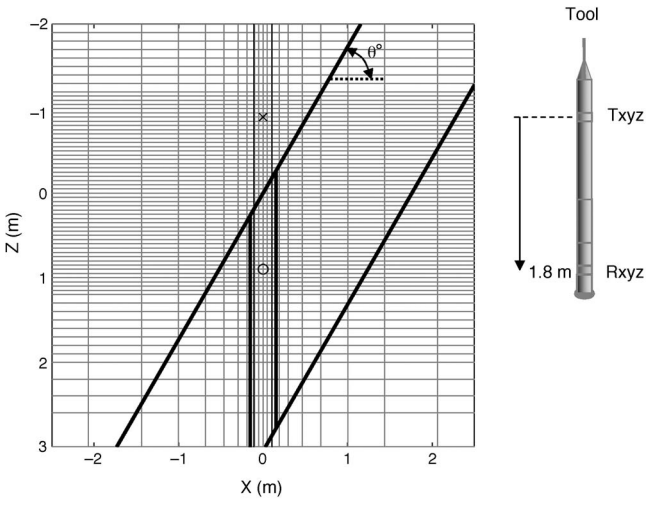

Figure 3. Subset of the $28 \times 28 \times 92$ grid used for the numerical simulations with coupled scalar-vector potentials. Overlain on the grid are the borehole and the first layer, with invasion, and dipping at 60°. The tool configuration is depicted to the right of the grid, roughly to scale and vertically aligned with the grid.

baugh, 2001). The 1D solution does include the effect of electrical anisotropy in the shale layers described in Figure 2. These results indicate an excellent agreement between the 3D and 1D solutions for the three frequencies considered in the simulations.

A subsequent 2D simulation performed for the model shown in Figure 2 assumes a vertical borehole and electrically isotropic shoulder beds. However, the 2D simulation does include the effect of radial invasion in the sand layers shown in Figure 2. The simulated Hzz quadrature field responses shown in Figure 6 indicate excellent agreement between the 3D coupled scalar-vector potential algorithm and the 2D FD solution (Gao, 2005).

To conclude the benchmarking exercises, we perform simulations for the 3D model shown in Figure 2 along a 60° borehole trajectory. The results presented in Figure 7 show, in general, good agreement between the 3D coupled scalar-vector potential algorithm and a 3D integral equation solution obtained with the algorithm of Fang et al. (2003).

In examining the influence of shoulder-bed anisotropy, Figure 8 shows simulation results for the model in Figure 2 for cases of isotropic and anisotropic shoulder beds, and with borehole dip angles of 30° and 60°. Quadrature Hzz, Hxx, and Hyy responses across the upper, 80 ohm-m reservoir layer show negligible differences between the isotropic and anisotropic cases at both 30° and 60° dip angles. Across the middle, 10 ohm-m reservoir layer, the 60° dip Hzz response peak slightly broadens; conversely, a significant narrowing of the peak is observed across the lower, 0.3 ohm-m layer. The quadrature Hxx and Hyy responses show similar changes between the isotropic and anisotropic cases across the middle reservoir layer, where a slight shift toward positive is observed at the 30° dip angle and negligible differences at the 60° angle. Across the bottom, 0.3 ohm-m reservoir layer, the effect on the Hxx quadrature response is a slight shift toward positive for both 30° and 60° dip angles; by contrast, the Hyy quadrature response exhibits a slight negative shift for the 30° and a significant negative shift for the 60° dip angle.

Given the significant shoulder-bed anisotropy effects observed across the bottom reservoir layer at the 60° dip angle, we simulated the case where the tool is centered across the layer, with responses calculated for increasing values of radial length of invasion. Figure 9a shows 25 kHz Hzz quadrature field responses versus radial length of invasion for the model with isotropic and anisotropic shoulder beds. A significant linear shift toward negative is observed at radial lengths of invasion less than 50 cm, beyond which the deviation between the two responses increases. In Figure 9b, the 25 kHz Hxx and Hyy quadrature responses significantly differ in their effects from the shoulder-bed anisotropy. There is a slight negative shift in the Hxx response out to roughly 60 cm of radial length of invasion, beyond which the deviation increases. By contrast, the change in the Hyy quadrature response is nonlinear across the entire range of radial length of invasion, with a large deviation peak toward positive occurring at approximately 60 cm.

DISCUSSION

Most of the algorithms available for the FD simulation of borehole EM measurements are based on the so-called electric/magnetic field formulation. The corresponding governing equation for the electric field given by Hou and Torres-Verdín (2003) is

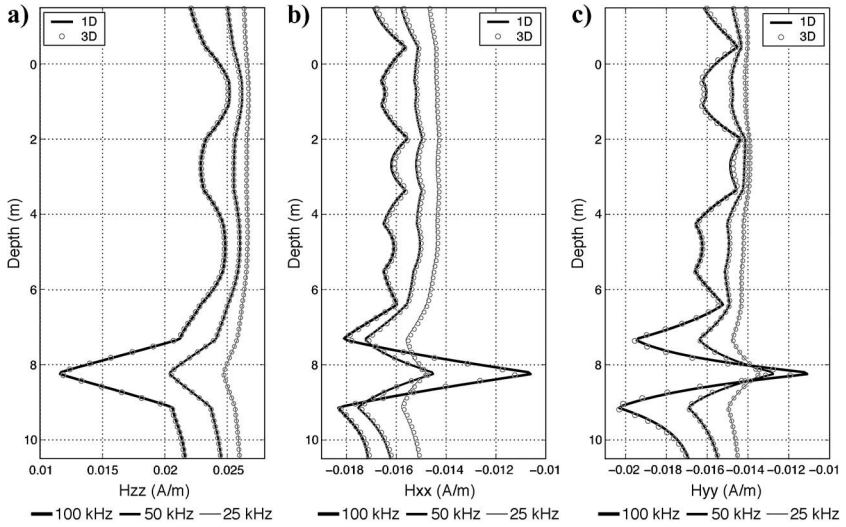

Figure 4. In-phase field response to the model shown in Figure 2, but with no borehole and invasion (1D simulation), for (a) Hzz, (b) Hxx, and (c) Hyy. Receiver offset is 1.8 m, and the measurement profile is 60° from normal to the layers. Depth is measured normal to the layers, from the top of layer 2 to the midpoint of the transmitter-receiver offset. Plots show 3D finite-difference (circles) and 1D analytical (solid lines) results for 100, 50, and 25 kHz.

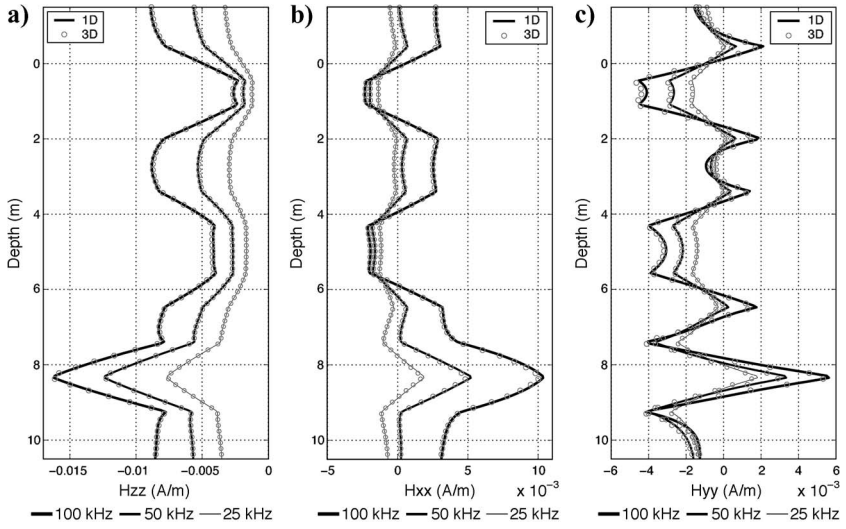

Figure 5. Quadrature field response for the model shown in Figure 2 with no borehole and invasion (1D simulation), for (a) Hzz, (b) Hxx, and (c) Hyy. Receiver offset is 1.8 m, and the measurement profile is 60° from the normal to the layers. Depth is measured normal to the layers, from the top of layer 2 to the midpoint of the transmitter-receiver offset. Plots show 3D coupled scalar-vector potential (circles) and 1D analytical (solid lines) results for 100, 50, and 25 kHz.

$$\nabla \times \nabla \times \mathbf{E} + i\omega\mu_0\bar{\bar{\sigma}}'\mathbf{E} = -i\omega\mu_0\mathbf{J}_p. \quad (15)$$

Discretization of equation 15 with central finite differences on Yee's staggered grid and enforcement of homogeneous Dirichlet boundary conditions ($\mathbf{n} \times \mathbf{E}|_{\partial\Omega} = 0$) yields a sparse complex system of linear equations given by

$$\mathbf{F}_e\mathbf{X}_e = \mathbf{O}_e, \quad (16)$$

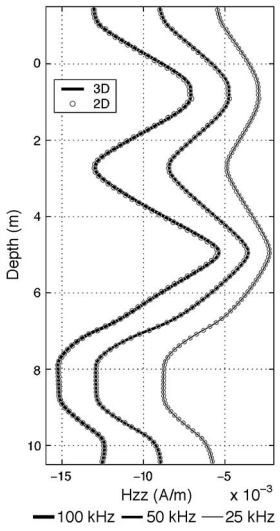

Figure 6. Quadrature Hzz field response for the model shown in Figure 2 with the borehole normal to the layers (2D simulation). Receiver offset is 1.8 m. Depth is measured normal to the layers, from the top of layer 2 to the midpoint of the transmitter-receiver offset. Plots show 3D coupled scalar-vector potential (lines) and 2D (symbols) finite-difference results for 100, 50, and 25 kHz.

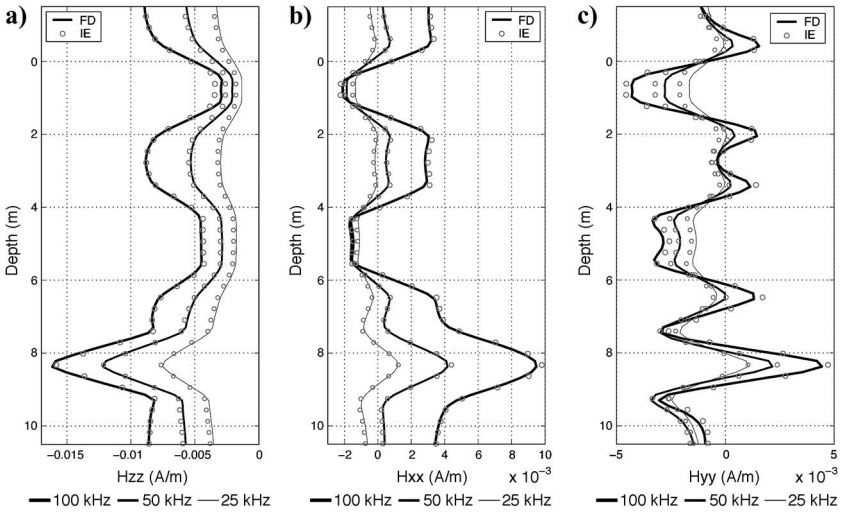

Figure 7. Quadrature field response for the model shown in Figure 2 for (a) Hzz, (b) Hxx, and (c) Hyy. Receiver offset is 1.8 m, and the borehole dip angle is 60° from the normal to the layers. Depth is measured normal to the layers, from the top of layer 2 to the midpoint of the transmitter-receiver offset. Plots show 3D coupled scalar-vector potential (solid lines) and 3D integral equation (circles) results for 100, 50, and 25 kHz.

where $\mathbf{F}_e = (a_{ij}^e)_{N_e \times N_e}$ is the matrix of coefficients, $\mathbf{N}_e$ is the total number of unknowns, $\mathbf{X}_e = (\mathbf{E}_x, \mathbf{E}_y, \mathbf{E}_z)^T$ is the solution vector, and $\mathbf{D}_e = (\mathbf{d}_x^e, \mathbf{d}_y^e, \mathbf{d}_z^e)^T$ is the right-hand side vector.

For the case of the coupled scalar-vector potential formulation, when $f = 0$, equations 6 and 7 reduce to standard dc potential equations. Therefore, in principle the same equations can be used to approach the solution of EM problems in the low-frequency regime without adjustments. Conversely, when $f = 0$, equation 15 reduces to $\nabla \times \nabla \times \mathbf{E} = 0$ or $\mathbf{F}_e\mathbf{X}_e = 0$. In such a case, there exists a null space of the solution vector $\mathbf{X}_e$, which maps the solution to zero; hence, matrix $\mathbf{F}_e$ becomes singular. For all Krylov subspace iterative solvers, convergence rates toward the true solution largely depend on the matrix condition number. Matrices with small condition numbers tend to converge rapidly, whereas those with large condition numbers (as in the cases of EM formulations here) converge slowly. Thus attempts to solve EM problems numerically using direct EM field methods result in a decrease in the speed of computation as the frequency approaches the dc limit. One way to overcome this problem is to precondition the EM field solution with a direct dc solver (Druskin et al., 1999). By contrast, the coupled scalar-vector potential formulation naturally takes care of such a situation with the implicit interplay between the vector and scalar functions included in equations 6 and 7.

For the potential formulation, one needs to solve four-coupled PDEs, whereas for the direct field formulation, only three coupled PDEs are included in the solution. Thus, the potential formulation requires larger computer storage than the EM field formulations. Another salient feature of the total electric or magnetic field formulations in the quasi-static regime is that they can be used to simulate multifrequency problems at almost the same cost of a single frequency simulation if approached with the spectral Lanczos decomposition method (Druskin et al., 1999, and Wang and Fang, 2001). This is not possible with a coupled scalar-vector potential formulation: Each frequency simulation needs to be performed separately. For large values of frequency, however, the quasi-static approximation is no longer valid and electric-field formulations do require that the solution be obtained separately for each frequency.

In summary, based on the discussion above, it follows that the major benefit of the coupled scalar-vector potential formulation is that the associated algorithmic implementation is general, regardless of frequency, presence of electrical anisotropy, and geometric description of the electrical-conductivity medium. An obvious disadvantage of coupled scalar-vector potential formulations over direct EM formulations is the larger memory storage requirements because of relatively larger unknown vectors, thereby increasing computation times. The numerical experiments reported in this paper show that a 50-point, single-frequency, single-source log profile, with an FD grid consisting of $28 \times 28 \times 92$ nodes can be simulated in approximately 1.9 hours of CPU time on an Intel Pentium 4 CPU 3.2-GHz personal computer furbished with 1 Gbyte of RAM.

To illustrate the algorithmic benefits of the coupled scalar-vector potential formulation, Figure 10 shows simulation results obtained over a broad frequency range for a fixed measurement point in a whole-space having a wide range of

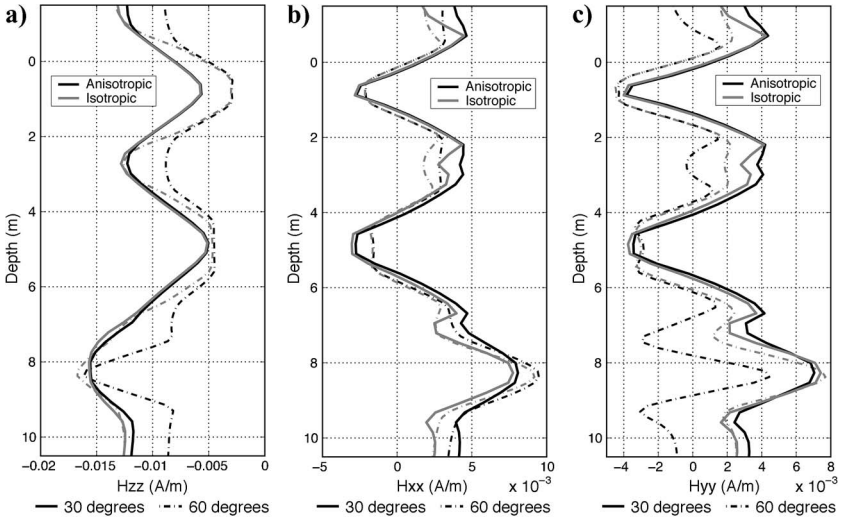

Figure 8. Quadrature field response for the model shown in Figure 2 for (a) Hzz, (b) Hxx, and (c) Hyy. Receiver offset is 1.8 m, and the frequency is 100 kHz. Depth is measured normal to the layers, from the top of layer 2 to the midpoint of the transmitter-receiver offset. Plots show results for borehole dip angles of 30° and 60° from the normal to the layers, with layers 1, 3, 5, and 7 being electrically anisotropic (black lines) and isotropic (gray lines).

conductivities. These results were obtained using the same FD grid for all conductivity and frequency values considered in the plots. The grid used is similar to that of previous simulations. However, to accommodate the small skin depths at the higher frequencies and conductivities, the grid was scaled down by a factor of 10 and was extended in size to the outer boundary located 1 to 1.5 skin depths away from the transmitter and receiver to accommodate for the largest skin-depth considered. Moreover, the transmitter-receiver separation was reduced to 0.5 m to decrease grid dimensions. Figure 10a and b shows the Hzz in-phase and quadrature field responses, respectively, in the frequency range from 10 kHz to 10 MHz for whole-space conductivity values ranging from 100 to 0.01 S/m. These plots indicate excellent agreement between the 3D coupled scalar-vector potential formulation (symbols) and the corresponding analytical (lines) solutions. More importantly, the results emphasize the flexibility and generality of the coupled sca-

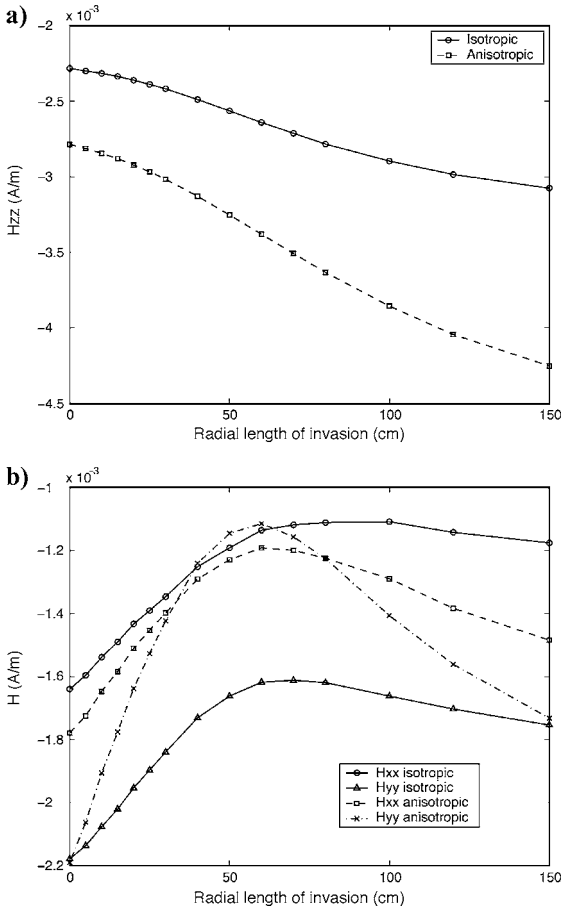

Figure 9. (a) Hzz and (b) Hxx and Hyy quadrature field response versus radial length of invasion for the 3D model shown in Figure 2, with and without electrical anisotropy. Receiver offset is 1.8 m and the tool is centered in the 0.3 ohm-m layer. The well dip angle is 60°. Depth is measured normal to the layers, from the top of layer 2 to the midpoint of the transmitter-receiver offset.

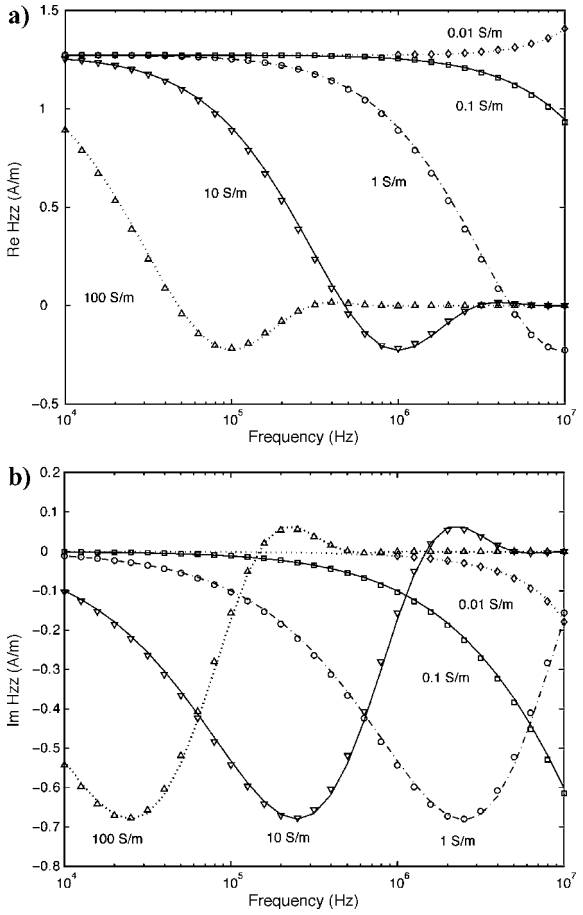

Figure 10. (a) In-phase and (b) quadrature Hzz response versus frequency in the presence of a whole-space of dielectric constant equal to 30. Transmitter-receiver offset is 0.5 m. The plots describe analytical (lines) and finite-difference (symbols) results for different whole-space conductivities, ranging from 100 to 0.01 S/m.

lar-vector potential formulation to produce accurate and efficient results over a wide range of frequencies.

CONCLUSIONS

The numerical results reported in this paper indicate that the new 3D coupled scalar-vector potential formulation is efficient and accurate to simulate cases of relatively large conductivity contrasts from dc to MHz on a personal computer. Our numerical examples show that a 50-point single-source, single-frequency log profile with an FD grid consisting of $28 \times 28 \times 92$ nodes can be simulated in approximately 1.9 hours of CPU time on an Intel Pentium 4 CPU 3.2-GHz personal computer furbished with 1 Gbyte of RAM. However, we also note that the scalar-vector formulation requires additional computer storage compared to that of direct EM field formulations. Benchmarking exercises indicate that the accuracy of our simulations is better than 1%, depending on the design of the FD grid.

The main conclusion from our study is that the coupled scalar-vector potential equations provide a general algorithmic formulation that is reliable, efficient, and accurate to simulate complex 3D borehole EM simulation problems that involve a wide range of frequencies and arbitrary cases of electrical anisotropy.

ACKNOWLEDGMENTS

The work reported in this paper was funded by the University of Texas at Austin's Research Consortium on Formation Evaluation, jointly sponsored by Anadarko Petroleum Corporation, Baker Atlas, BP, ConocoPhillips, ENI E&P, ExxonMobil, Halliburton Energy Services, the Mexican Institute for Petroleum, Occidental Petroleum Corporation, Petrobras, Precision Energy Services, Schlumberger, Shell International E&P, Statoil, and TOTAL. We express our gratitude to the above organizations. The authors also wish to thank Tsili Wang, Sheng Fang, Ian Zhang, and Guozhong Gao for fruitful discussions and valuable comments on the research work presented in this paper. A note of special gratitude goes to David Alumbaugh and one anonymous reviewer for their constructive technical and editorial feedback.

APPENDIX A

COMPARISON OF DIFFERENT PRECONDITIONING METHODS

We implemented the solution of the linear system described by equation 12 using the CBCG method with different preconditioning methods, including Jacobi, SSOR, and ILU (Axelsson, 1994). Based on extensive numerical tests (see Figures A-1 and A-2), we found that the SSOR preconditioning strategy exhibited faster convergent rates than Jacobi preconditioning. We recall that the use of an SSOR preconditioner requires a specific choice of acceleration rate, OMEGA. Numerous tests indicated that the choice OMEGA = 1.0 ensured acceptable convergence rates for all the examples considered in this paper.

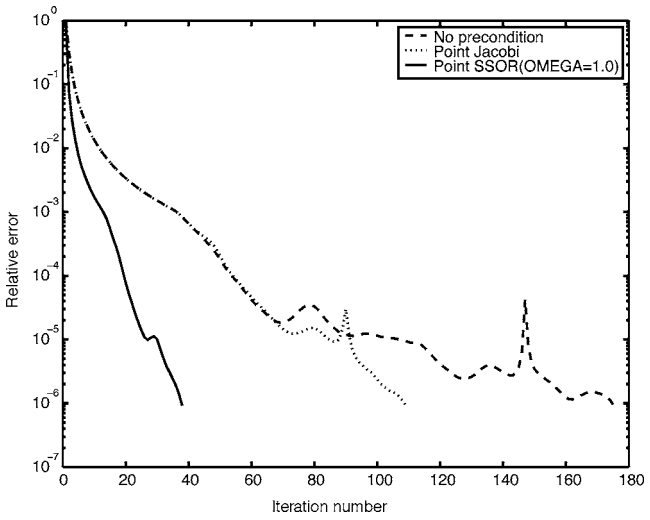

Figure A-1. Comparison of iterative errors for the CBCG algorithm using different preconditioning methods for the case of 3D layered anisotropic media with borehole.

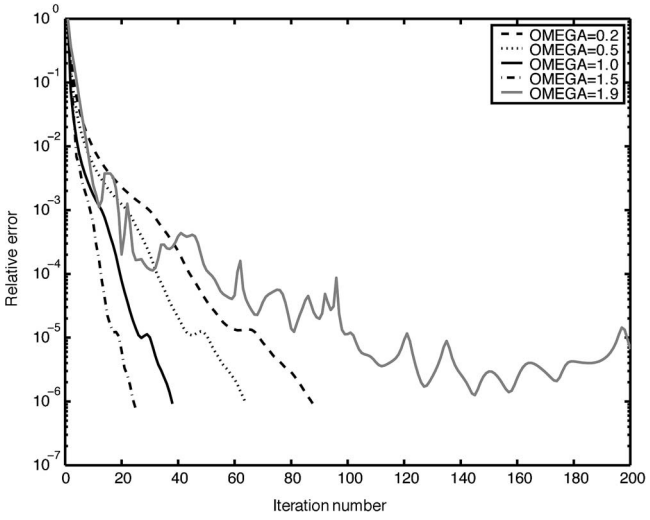

Figure A-2. Comparison of iterative errors for the CBCG iterative algorithm using different values of OMEGA in conjunction with the SSOR preconditioner for the case of 3D layered anisotropic media with borehole.

REFERENCES

Axelsson, O., 1994, Iterative solution methods: Cambridge University Press.

Davydycheva, S., V. Druskin, and T. Habashy, 2003, An efficient finite-difference scheme for electromagnetic logging in 3D anisotropic inhomogeneous media: Geophysics, **68**, 1525–1536.

Druskin, V., L. Knizhnerman, and P. Lee, 1999, New spectral Lanczos decomposition method for induction modeling in arbitrary 3-D geometry: Geophysics, **64**, 701–706.

Fang, S., G. Gao, and C. Torres-Verdín, 2003, Efficient 3-D electromagnetic modeling in the presence of anisotropic conductive media using integral equations: Three-Dimensional Electromagnetics Workshop No. 3 (3DEM-3), Extended Abstracts.

Gao, G., 2005, Simulation of borehole electromagnetic measurements in dipping and anisotropic rock formations and inversion of array induction data: Ph.D. dissertation, The University of Texas at Austin.

Haber, E., and U. M. Ascher, 2001, Fast finite volume simulation of 3D elec-

tromagnetic problems with highly discontinuous coefficients: SIAM Journal on Scientific Computing, **22**, 1943–1961.
Haber, E., U. M. Ascher, and D. W. Oldenburg, 2000, Fast simulation of 3D electromagnetic problems using potentials: Journal Computational Physics, **163**, 150–171.
——–, 2002, 3D forward modeling of time domain electromagnetic data: 72nd Annual International Meeting, SEG, Expanded Abstracts, 641–644.
Hou, J., and C. Torres-Verdín, 2003, Finite-difference modeling of EM fields using coupled potentials in 3D anisotropic media: Application to borehole logging: 73rd Annual International Meeting, SEG, Expanded Abstracts, 522–525.
King, R. W. P., and S. Prasad, 1986, Fundamental electromagnetic theory and applications: Prentice-Hall, Inc.
LaBrecque, D. J., 1999, Finite difference modeling of 3-D EM fields with scalar and vector potentials, *in* M. Oristaglio and B. Spies, eds., Three-dimensional electromagnetics: SEG, 146–160.
Lu, X., and D. L. Alumbaugh, 2001, One-dimensional inversion of three-component induction logging in anisotropic media: 71st Annual International Meeting, SEG, Expanded Abstracts, 376–379.
Moskow, S., V. Druskin, T. Habashy, P. Lee, and S. Davydycheva, 1999, A finite difference scheme for elliptic equations with rough coefficients using a Cartesian grid nonconforming to interfaces: SIAM Journal on Numerical Analysis, **36**, 442–464.
Newman, G. A., and D. L. Alumbaugh, 2002, Three-dimensional induction logging problems, part 2: A finite difference solution: Geophysics, **67**, 484–491.
Smith, J. T., 1996, Conservative modeling of 3-D electromagnetic fields, Part II: Biconjugate gradient solution and an accelerator: Geophysics, **61**, 1319–1324.
van Bladel, J., 1985, Electromagnetic fields: Hemisphere Publishing Corporation.
Wang, T., and S. Fang, 2001, 3-D electromagnetic anisotropy modeling using finite differences: Geophysics, **66**, 1386–1398.
Weiss, C. J., and G. A. Newman, 2002, Electromagnetic induction in a fully 3-D anisotropic earth: Geophysics, **67**, 1104–1114.
——–, 2003, Electromagnetic induction in a generalized 3D anisotropic earth, part 2: The LIN preconditioner: Geophysics, **68**, 922–930.
Yee, K. S., 1966, Numerical solution of initial boundary value problems involving Maxwell's equations in isotropic media: IEEE Transactions on Antennas and Propagation, **AP-14**, 302–307.